Monthly Notices
of the
ROYAL ASTRONOMICAL SOCIETY

MNRAS **497,** 81–93 (2020)
Advance Access publication 2020 June 24

doi:10.1093/mnras/staa1816

An EAGLE's view of *ex situ* galaxy growth

Thomas A. Davison [1,2,3★] Mark A. Norris [1] Joel L. Pfeffer [4] Jonathan J. Davies [4] and Robert A. Crain [4]

[1]*Jeremiah Horrocks Institute, University of Central Lancashire, Preston PR1 2HE, UK*
[2]*European Southern Observatory, Karl-Schwarzschild-Strasse 2, D-87548 Garching bei Muenchen, Germany*
[3]*Isaac Newton Group of Telescopes, E-38700 Santa Cruz de La Palma, Spain*
[4]*Astrophysics Research Institute, Liverpool John Moores University, 146 Brownlow Hill, Liverpool L3 5RF, UK*

Accepted 2020 June 14. Received 2020 June 12; in original form 2019 November 13

ABSTRACT

Modern observational and analytical techniques now enable the direct measurement of star formation histories and the inference of galaxy assembly histories. However, current theoretical predictions of assembly are not ideally suited for direct comparison with such observational data. We therefore extend the work of prior examinations of the contribution of *ex situ* stars to the stellar mass budget of simulated galaxies. Our predictions are specifically tailored for direct testing with a new generation of observational techniques by calculating *ex situ* fractions as functions of galaxy mass and morphological type, for a range of surface brightnesses. These enable comparison with results from large field of view (FoV) Integral Field Unit (IFU) spectrographs, and increasingly accurate spectral fitting, providing a look-up method for the estimated accreted fraction. We furthermore provide predictions of *ex situ* mass fractions as functions of galaxy mass, galactocentric radius, and environment. Using $z = 0$ snapshots from the 100 and 25 cMpc^3 EAGLE (Evolution and Assembly of GaLaxies and their Environments) simulations, we corroborate the findings of prior studies, finding that *ex situ* fraction increases with stellar mass for central and satellite galaxies in a stellar mass range of 2×10^7 to 1.9×10^{12} M$_\odot$. For those galaxies of mass $M_* > 5 \times 10^8$ M$_\odot$, we find that the total *ex situ* mass fraction is greater for more extended galaxies at fixed mass. When categorizing satellite galaxies by their parent group/cluster halo mass, we find that the *ex situ* fraction decreases with increasing parent halo mass at fixed galaxy mass. This apparently counterintuitive result may be due to high passing velocities within large cluster haloes inhibiting efficient accretion on to individual galaxies.

Key words: galaxies: evolution – galaxies: interactions – galaxies: structure.

1 INTRODUCTION

The recent simultaneous advancement of improved observational technology and stunningly detailed theoretical simulations has significantly expanded and deepened the scientific repertoire available to study galaxy formation.

One of the key insights inferred from large cosmological simulations of galaxy formation (e.g. the EAGLE, Illustris, Horizon-AGN, and Fire simulations; Dubois et al. 2014; Hopkins et al. 2014; Vogelsberger et al. 2014a, b; Crain et al. 2015; Schaye et al. 2015) is that galaxies (particularly massive elliptical galaxies) undergo a 'two-phase' process of assembly (see e.g. Oser et al. 2010), in which they initially form a relatively compact core of stars formed *in situ* to the main progenitor from infalling cosmological cold gas and gas returned to the interstellar medium by stellar evolution. Following this period (at $z \lesssim 3$; Oser et al. 2010), simulations indicate continuing accretion of stars from smaller galaxies outside of the virial radius via mergers and tidal stripping, resulting in a build-up of *ex situ* stars. These simulations indicate that the *ex situ* fraction is a strong function of the mass and formation history of the galaxy, with galaxies of $M_* = 10^9$ M$_\odot$ being almost entirely composed of stars formed *in situ*, while in contrast ≈90 per cent of the stellar mass of the most massive galaxies ($M_* > 1.7 \times 10^{11}$ M$_\odot$) can have originated in previously distinct progenitors (Oser et al. 2010; Lackner et al. 2012; Rodriguez-Gomez et al. 2016; Pillepich et al. 2018).

Observational evidence has accumulated to support the two-mode scenario of *in situ* and *ex situ* stellar assembly from a variety of sources. The most obvious is the observation that many galaxies, if not most, including our own Milky Way, exhibit streams of stars attributable to the remains of tidally disrupted dwarf galaxies (see e.g. Belokurov et al. 2006; Martínez-Delgado et al. 2008; Jennings et al. 2015; Hood et al. 2018). Examination of the distribution and orbits of globular clusters (GCs) has shown that the two GC subpopulations typically found around massive galaxies can be associated with the two phases: metal-rich GCs with the *in situ* burst of formation in the main progenitor and metal-poor GCs with the later accretion of lower mass galaxies hosting lower metallicity GC systems (e.g. Forbes et al. 2011; Romanowsky et al. 2012; Pota et al. 2015; Beasley et al. 2018; Kruijssen et al. 2018; Fahrion et al. 2020). Investigations of the radial gradients of stellar populations in massive early-type galaxies show that the outskirts of such galaxies are composed of older, lower metallicity, alpha-enhanced stars indicative of accretion from lower mass progenitors (e.g. Greene et al. 2012; La Barbera et al. 2012; Martin et al. 2018). The same mode of galaxy assembly has also been suggested by independent observational means such as

★ E-mail: tdavison@uclan.ac.uk

supermassive black hole growth (Krajnović, Cappellari & McDermid 2018). Finally, observations indicate that at earlier epochs galaxies were considerably more compact than galaxies of comparable mass today, an observation that can in part be explained by the later addition of accreted stars to the outer regions of galaxies (van der Wel et al. 2014; van Dokkum et al. 2014).

Recently, observational technology and analytical techniques have advanced sufficiently that the opportunity now exists to infer in detail the star formation and mass assembly histories of galaxies on an individual basis. This advancement is largely due to three developments:

(i) The advent of integral field spectrographs with a large field of view ($\gtrsim$1 arcmin; e.g. SAURON at the WHT, GCMS on the 2.7 m Harlan J. Smith telescope, and MUSE at the VLT, Bacon et al. 2001, 2010; Hill et al. 2008). These and similar instruments enable the simultaneous measurement of high signal-to-noise spectra out to large galactocentric distances, delivering unprecedented spatially resolved measurements of spectroscopically derived stellar population parameters across galaxies (see e.g. Guérou et al. 2016; Mentz et al. 2016).

(ii) The development of full spectral fitting methods (e.g. PPXF, STARLIGHT, VESPA, etc.; Cappellari & Emsellem 2004; Cid Fernandes et al. 2005; Tojeiro et al. 2007; Cappellari 2017) to extract temporally resolved star formation histories from the integrated light measurements made by spectrographs (see e.g. Onodera et al. 2012; Norris et al. 2015; Ferré-Mateu et al. 2017; Kacharov et al. 2018; Ruiz-Lara et al. 2018, for demonstrations of the application of this approach).

(iii) The development of techniques to use the information provided by the full star formation and chemical enrichment histories provided by (ii) to infer galaxy accretion histories (Boecker et al. 2019; Kruijssen et al. 2019) or to provide additional constraints on assembly history in combination with kinematic information (e.g. a population-dynamical approach; Poci et al. 2019).

In order to aid the understanding of the huge quantity of information provided by the combination of these technologies and techniques, it is necessary to have more detailed predictions from simulations with which to compare to the observations. To date, most studies of the assembly histories of galaxies have focused on examining the underlying physics from a more theoretical direction (e.g. Oser et al. 2010; Rodriguez-Gomez et al. 2016; Qu et al. 2017). In this paper, we use the EAGLE (Evolution and Assembly of GaLaxies and their Environments) simulations to develop predictions for the fraction of stars that formed *in situ* and *ex situ*, in terms of observable quantities most useful to observers, e.g. galaxy stellar mass, galaxy type (roughly early or late type), environment (specifically halo mass), and, most usefully, surface brightness. This study therefore builds on that of Qu et al. (2017) whose analysis of EAGLE found that, typically, galaxies of mass $M_* < 10^{10.5}$ M$_\odot$ assemble less than 10 per cent of their mass from *ex situ* sources, while those of $M_* > 10^{11}$ M$_\odot$ typically exhibit *ex situ* mass fractions of $\sim$20 per cent (though with a large scatter in these values).

This paper is organized as follows. In Section 2, we describe the EAGLE simulations we are utilizing, as well as the methodology for classifying star particles as *in situ* or *ex situ*. In Section 3, we present the results of our investigation of the dependence of *in situ* and *ex situ* mass fractions as functions of various observable properties of galaxies, and of galactocentric radius. Furthermore, we provide tabulated data for use when comparing to observational studies. In Section 4, we discuss some of the implications of our results in light of expectations and previous studies. Finally, in Section 5 we provide some concluding remarks.

2 METHODOLOGY

2.1 Overview of simulations

The EAGLE simulations are a suite of cosmological hydrodynamical simulations created with the aim of understanding the coevolution of galaxies and supermassive black holes within a cosmologically representative volume of a standard Lambda cold dark matter Universe. For a more comprehensive overview of the full suite of simulations, see Schaye et al. (2015) and Crain et al. (2015).

For this work, we focus on two simulations, Recal-L025N0752 (hereafter Recal-025) and Ref-L0100N1504 (hereafter Ref-100). The Ref-100 simulation is a periodic volume, 100 cMpc on a side, realized with 1504^3 dark matter particles and an initially equal number of gas particles, described as 'intermediate resolution'. The resultant initial baryonic particle mass is 1.81×10^6 M$_\odot$, the dark matter particle mass is 9.70×10^6 M$_\odot$, and the gravitational softening length is 2.66 ckpc (comoving kiloparsecs) limited to a maximum proper length of 0.7 pkpc (proper kiloparsecs).

Subgrid feedback parameters were calibrated to ensure $z = 0$ reproduction of the galaxy stellar mass relation, disc sizes, and the $M_{\rm BH}$–M_* relation. Further studies make comparisons to other observational properties, showing close matches (Furlong et al. 2015; Lagos et al. 2015; Schaye et al. 2015). Detailed descriptions of the calibration procedure and the influence of parameter variation are given by Crain et al. (2015).

Recal-025 has the higher resolution of the two simulations and the parameters of the Recal model were recalibrated to achieve a similarly good match to the observational data as the reference model. This simulation is 25 cMpc on a side, realized with 752^3 dark matter and gas particles. The resultant initial baryonic particle mass is 2.26×10^5 M$_\odot$, the dark matter particle mass is 1.21×10^6 M$_\odot$, and the gravitational softening length is 1.33 ckpc limited to a maximum proper length of 0.35 pkpc.

The EAGLE simulations use a Chabrier initial stellar mass function (Chabrier 2003) and was run with a modified version of the GADGET-3 smoothed particle hydrodynamics code. The subgrid treatments are well explained in McAlpine et al. (2016).

For our analysis, we focus on the final $z = 0$ snapshots for both simulations, where the simulated galaxies are comparable to local galaxies (see e.g. Schaye et al. 2015; Trayford et al. 2015). These specific simulations are chosen for their complementary ability to adequately resolve the formation of lower mass ($M < 10^9$ M$_\odot$) galaxies (Recal-025), and to provide sufficient statistics on the properties of rarer high-mass galaxies (Ref-100). We limit our analyses to only those galaxies that contain a minimum count of >500 bound stellar particles at $z = 0$, to ensure reasonable sampling errors on derived properties.

2.2 *In situ*/*ex situ* classification

The classification of any simulated star (or dark matter) particle as '*in situ*' or '*ex situ*' is a matter of some debate in the literature, with several schemes implemented to date (see e.g. Oser et al. 2010; Pillepich, Madau & Mayer 2015; Rodriguez-Gomez et al. 2016; Qu et al. 2017; Clauwens et al. 2018; Monachesi et al. 2019). In this work, we implement a scheme to classify each particle as described below.

In common with most modern cosmological simulations, the EAGLE simulations track galaxy merger histories by post-processing halo and subhalo catalogues to produce 'merger trees'. The structures are connected at different epochs using the D-Trees algorithm (Jiang et al. 2014) that tracks linked particles to identify progenitors and descendants. As galaxies merge, the total mass of each branch forming that galaxy is summed, and the larger branch mass is defined as the 'main progenitor'.

In our scheme, the subhalo that an initial gas particle is a member of (if any) in the snapshot immediately before conversion to a star particle is identified. Following this, the unique identifier of that progenitor, as determined by the merger tree, is assigned to the particular star particle. If the particle happens to be unbound at that snapshot, the earliest snapshot after star formation in which the particle resides in a subgroup as a member is defined as its host.

We then compare the particle progenitor identifier to the identifier of the subhalo the particle is a member of at $z = 0$. If the subhalo at the snapshot prior to star formation is in the main branch of the final galaxy, the particle is considered *in situ*. If the progenitor galaxy is not in the main branch, it is defined as *ex situ*.

The result is that each of the particles comprising a simulated galaxy at $z = 0$ has a flag denoting the nature of its origin. This is performed for all particles and data can be limited to a chosen aperture as usual along with other properties. In addition to this flag, and to the standard properties recorded for each EAGLE particle in its snapshot (e.g. stellar mass, metallicity, coordinates), we also calculate the distance from the galaxy centre (defined by the position of the minimum of the gravitational potential, itself the position of the most bound particle) for each particle. From this information, it is trivial to compute spherically averaged stellar half-mass radii ($r_{1/2}$). This can be achieved simply by summing stellar particles in order of absolute distance to the galaxy centre until half the total mass within a chosen aperture (in this study, 100 pkpc) has been reached. Using this information, it is then possible to search for correlations between *in situ* and *ex situ* fraction and a host of final galaxy properties.

Combining the status of the particle origin with other EAGLE particle properties allows us to mask to *in situ* or *ex situ* stars. We use this to examine ensemble properties as a function of radius, stellar mass, and halo mass for individual galaxies.

2.3 Galaxy properties and classification

A further property that is of interest to observers is the morphological type of galaxy under study. This is especially true in this work as morphological transformation has long been thought to be related to merger history (see e.g. Querejeta et al. 2015; Martin et al. 2018), and in fact the addition of *ex situ* stars is suggested as the main mode of mass assembly for large early-type galaxies (Martin et al. 2018).

Using the corotational stellar energy parameter $\kappa_{\rm co}$ made available as part of the EAGLE data release (see e.g. Thob et al. 2019) for each galaxy in the simulations, we separate galaxies into the 'blue sequence' of discy star-forming galaxies ($\kappa_{\rm co} > 0.4$) and 'red sequence' of more spheroidal passively evolving galaxies ($\kappa_{\rm co} < 0.4$) as advocated by Correa et al. (2017). The method is based on earlier development in Sales et al. (2010) in which rotational energy is quantified as the fraction of kinetic energy invested in ordered rotation. However, the Correa et al. (2017) method instead uses corotational energy, defined as

$$\kappa_{\rm co} = \frac{K_{\rm co}^{\rm rot}}{K} = \frac{1}{K} \sum_{i, L_{z,i}>0} \frac{1}{2} m_i \left(\frac{L_{z,i}}{m_i R_i} \right)^2, \quad (1)$$

where ($L_{z,i} > 0$) defines all corotating stellar particles within 100 pkpc of the Galactic Centre, and R_i is the two-dimensional radius in the plane normal to the rotation axis. This is shown to be efficient in classifying galaxies in the EAGLE simulations.

As an independent check of this morphological classification, we also apply a separation based on specific star formation rate (sSFR). By plotting stellar mass versus sSFR for the EAGLE galaxy sample, a boundary sSFR of 0.01 $\rm Gyr^{-1}$ is found to effectively separate the blue sequence and red sequence. Applying this selection only alters the classification of 6.35 per cent of galaxies, relative to the $\kappa_{\rm co}$ selection, leading to no significant changes of any of our findings. Therefore, to maintain consistency with other studies using EAGLE simulations we use the $\kappa_{\rm co}$ classification in all further analyses.

2.4 The EAGLE galaxy sample

The histogram in the upper panel of Fig. 1 shows our final sample of EAGLE galaxies. Sharp discontinuities in the apparent distribution of galaxies are the result of the previously described lower particle limit of 500 stellar particles per galaxy. This equates to a minimum stellar mass within 100 pkpc of 4.01×10^7 and 3.48×10^8 $\rm M_\odot$ at $z = 0$ for the Recal-025 and Ref-100 simulations, respectively. The most massive galaxies in the two samples have mass 1.12×10^{11} (Recal-025) and 1.93×10^{12} $\rm M_\odot$ (Ref-100). As can clearly be seen, the Recal-025 and Ref-100 simulation sample different parts of the mass distribution, owing to their differing resolutions and volumes. Recal-025 provides high numbers of low-mass galaxies in the range $\sim 10^{7.5}$–$10^{9.5}$ $\rm M_\odot$, with the Ref-100 simulation taking over (with overlap) to provide galaxies in the range $\sim 10^{8.5}$–10^{12} $\rm M_\odot$. Though Recal-025 provides some small number of galaxies of mass $> 10^{9.5}$ $\rm M_\odot$, the fraction is barely noticeable compared to those provided by Ref-100.

The lower two panels of Fig. 1 show the distribution of objects across the mass–size plane. The half-mass radius is determined following the prescription provided in Section 2.2. These panels display observational best-fitting lines from Lange et al. (2015) produced for the Galaxy And Mass Assembly (GAMA) survey, in which M_*–$r_{1/2}$ relations are built for 'red' and 'blue' sequence galaxy samples using a double power-law function described by Shen et al. (2003)

$$r_{1/2} = \gamma \left(\frac{M_\star}{M_\odot} \right)^\alpha \left(1 + \frac{M_\star}{M_0} \right)^{\beta-\alpha}. \quad (2)$$

We choose to overplot the K-band fits due to the fact that the K band has been shown to be a good stellar mass tracer due to its relative insensitivity to both extinction and the effects of young hot stars which bias mass-to-light measurements in the optical (e.g. McGaugh & Schombert 2014; Norris et al. 2016). Hence, we expect that K should provide the closest match between the simulations that output stellar mass, and the observationally inferred values. The parameters for equation (2) are provided in Shen et al. (2003) for K band. For the blue sample, these parameters are $\gamma = 0.1$, $\alpha = 0.16$, $\beta = 1.00$, and $M_0 = 33.62 \times 10^{10}$ $\rm M_\odot$. Parameters for the red sample are $\gamma = 0.12$, $\alpha = 0.1$, $\beta = 0.78$, and $\rm M_0 = 2.25 \times 10^{10}$ $\rm M_\odot$.

As Fig. 1 demonstrates, the simulated galaxies appear to be slightly more extended at fixed mass than real galaxies. This has a number of potential explanations. One is the result of overefficient feedback within the EAGLE simulations (see e.g. Crain et al. 2015) that moves galaxies of fixed M_* into haloes of higher M_{200} potentially extending the galaxies. A second explanation is described in Ludlow et al. (2019), wherein if a simulation contains particle species of differing mass (such as the lower mass baryonic and higher mass dark matter

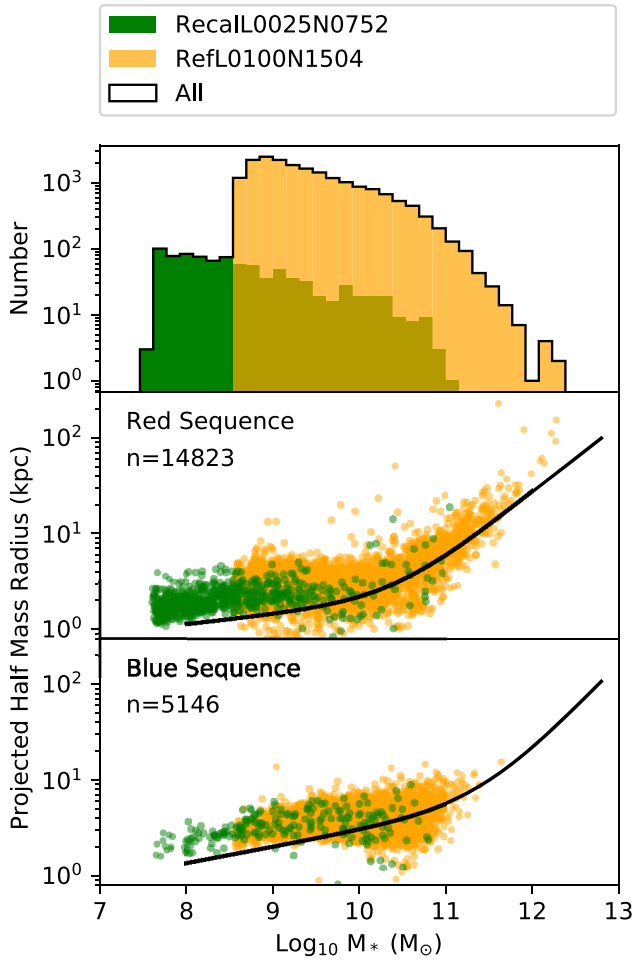

Figure 1. Origin of all objects used in subsequent mass–size plots. The upper panel shows a histogram of the mass distribution of simulated galaxies across the ($\log_{10}$) stellar mass axis. The centre and lower panels show the same distribution in the mass–size plane, with objects separated into red sequence and blue cloud populations, using the $\kappa_{\rm co}$ parameter (see Section 2.3). The radius shown is projected half-mass radius, averaged over the three orthogonal projections. Fit lines show the double power-law mass–size trend of the observed galaxy population in *K* band, as described in Lange et al. (2015). A similar figure for only the Ref-100 simulation can be found in Furlong et al. (2016) with comparison to measurements from van der Wel et al. (2014) and Shen et al. (2003).

particles in EAGLE), two-body scattering can be artificially inflated. This occurs when higher mass species effectively transfer kinetic energy to lower mass species, artificially raising their energy. This may contribute to the greater extent of the EAGLE galaxies compared to observation that we see in Fig. 1, especially in lower mass galaxies.

2.5 Summary of other quantities

Units and conversions are kept consistent with prior EAGLE analysis works. An aperture of 100 pkpc is considered for all objects unless otherwise stated. This ensures that galaxies of $M_* > 10^{11}$ M$_\odot$ are properly considered, as demonstrated in fig. 4 of Schaye et al. (2015). For subhalo mass units, only the baryonic stellar component is used; however, when analysing halo mass (such as in Section 3.1.3) we use the total mass within the corresponding group Crit200 radius, where group Crit200 defines the radius at which mass is equal to 200 times the critical mass of the Universe.

In order to use the EAGLE simulations to provide robust predictions for observational studies, we provide estimates of the *ex situ* mass fraction as a function of more readily observable quantities. To achieve this, each simulated galaxy is analysed to determine the *ex situ* fraction as a function of visual (i.e. *V* band) surface brightness. The results of this are discussed in Section 3.2.2

To estimate surface brightness quantities, galaxies are projected in the *xy* plane, effectively randomizing the viewing angle relative to the observer. This is intended to give an accurate representation of galaxies compared to real observing conditions. Each galaxy is set at a fiducial distance of 16.5 Mpc (the approximate distance to the Virgo cluster). Following this, the luminosity of each particle is calculated by matching each to interpolated stellar mass-to-light relations built from the single stellar population models of Maraston (2005).

Derivation of projected ellipticity is completed using the formulae described by Lagos et al. (2018). Here, *r*-band luminosity is used to calculate the projected ellipticity by

$$\epsilon = 1 - \sqrt{\frac{b^2}{a^2}}, \tag{3}$$

where

$$a^2 = \frac{\bar{x}^2 + \bar{y}^2}{2} + \sqrt{\left(\frac{\bar{x}^2 - \bar{y}^2}{2}\right)^2 + \bar{xy}} \tag{4}$$

$$b^2 = \frac{\bar{x}^2 + \bar{y}^2}{2} - \sqrt{\left(\frac{\bar{x}^2 - \bar{y}^2}{2}\right)^2 + \bar{xy}} \tag{5}$$

and

$$\bar{x}^2 = \frac{\sum_i L_i x_i^2}{\sum_i L_i} \tag{6}$$

$$\bar{y}^2 = \frac{\sum_i L_i y_i^2}{\sum_i L_i} \tag{7}$$

$$\bar{xy} = \frac{\sum_i L_i x_i y_i}{\sum_i L_i}, \tag{8}$$

in which L is the *r*-band luminosity, and x and y are the particle coordinates in the projected frame (with the centre of the galaxy set to 0,0). The position angle of the elliptical fit is given by

$$\theta_{\rm PA} = \frac{1}{2}\tan^{-1}\left(\frac{2\bar{xy}}{\bar{x}^2 - \bar{y}^2}\right). \tag{9}$$

Adaptive bins measure the luminosity of each galaxy from the centre outwards. Particles are binned in order of distance (weighted by ellipticity) from the centre, with every 75 particles justifying a new bin. Area and the sum of the luminosity of particles within each bin are calculated, allowing us to build a luminosity profile across the galaxy. Ellipse major axis positions, corresponding to the mid-point between integer magnitudes, are read from the luminosity profile (e.g. choosing inner and outer elliptical radii of 22.5 and 23.5 mag for a magnitude of 23). With these boundaries, we define new concentric elliptical bins with the total luminosity of particles contained in a bin providing magnitudes per square arcsecond. Using the previously described *ex* or *in situ* classification of each particle, we can then determine the *ex situ* fraction at any desired surface brightness value.

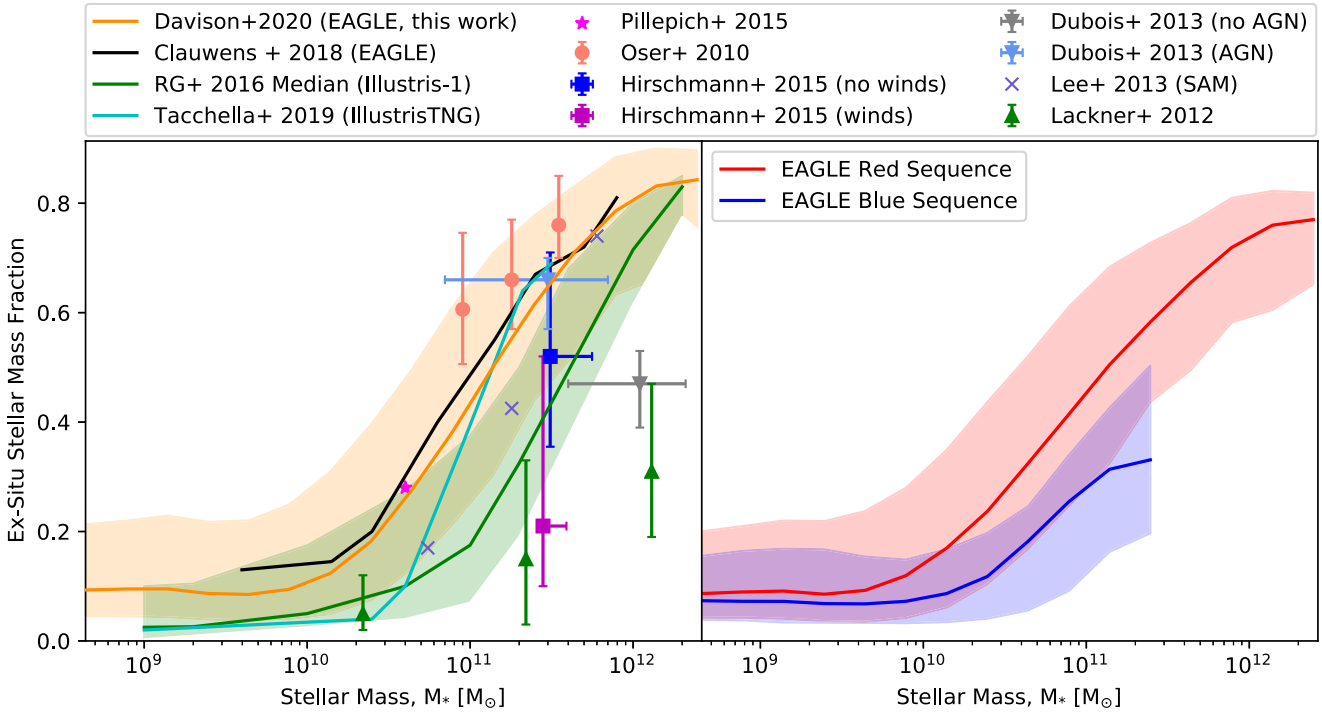

Figure 2. This figure (modelled after fig. 3 from Rodriguez-Gomez et al. 2016) shows *ex situ* fraction as a function of stellar mass and adds $z = 0$ EAGLE data for comparison. EAGLE data consist of a sample built from the Recal-025 and Ref-100 simulations as detailed in Fig. 1. The left-hand panel compares the full sample of EAGLE galaxies to previous studies. The right-hand panel separates the EAGLE sample into blue sequence and red sequence components using the $\kappa_{\rm co}$ parametrization. Shaded regions show 1σ percentile scatter in the *ex situ* plane. To reproduce accurately the Rodriguez-Gomez et al. (2016) figure, median *ex situ* fraction is calculated with 0.25 dex mass bins with a minimum bin population of 8 (the highest mass bin) and a maximum bin population of 3172. Only particles inside of 100 pkpc are considered.

3 RESULTS

3.1 *Ex situ* fraction as a function of galaxy properties

3.1.1 Ex situ fraction as a function of galaxy mass

In order to examine the reliability of our methodology, we first examine the dependence of *ex situ* fraction on various other properties. This allows us to compare to the results of previous studies, and therefore provides confidence in the reliability of our later predictions.

Fig. 2 displays the stellar mass dependence of the *ex situ* fraction for our EAGLE sample along with a selection of other literature sources. The layout follows that of fig. 3 of Rodriguez-Gomez et al. (2016) in which the same analysis is performed on simulated galaxies from the Illustris simulations (Genel et al. 2014; Vogelsberger et al. 2014a; Nelson et al. 2015).

As can be seen in Fig. 2, our sample exhibits the same overall trend as found by previous studies (Oser et al. 2010; Rodriguez-Gomez et al. 2016; Qu et al. 2017; Clauwens et al. 2018), in that *ex situ* fraction increases with increasing galaxy mass. In common with Qu et al. (2017), we find that EAGLE galaxies display systematically higher *ex situ* fractions than Illustris (Rodriguez-Gomez et al. 2016) at all stellar masses, though the two samples are consistent within their mutual scatters. IllustrisTNG displays almost identical results as EAGLE at high mass ($>2 \times 10^{11}$ M$_\odot$) (Tacchella et al. 2019). Our sample also displays only marginally lower *ex situ* fractions at fixed mass than either Oser et al. (2010) or Clauwens et al. (2018). The analysis of Clauwens et al. (2018) makes use of the same Ref-100 EAGLE simulation as this work, although it applies an independent method of classifying *in situ* and *ex situ* fraction. The fact that two independent methods for determining *ex situ* fraction agree so well, when looking at the same simulation, is encouraging.

The origins of the differences between the *ex situ* mass fractions of EAGLE and Illustris are explored by Qu et al. (2017), with the preponderance of the differences likely caused by differing stellar and active galactic nucleus (AGN) feedback treatment. Minor differences between values from our analysis and those of Clauwens et al. (2018) can be attributed to the systematic uncertainty associated with using differing methods to classify the origin of stars within a galaxy, such as assigning the particle to a progenitor galaxy prior to or after star formation occurs, as well as a difference in samples examined, with Clauwens et al. not including Recal-025 as we do. The fact that our results agree so closely with those found by several independent analyses of several independent simulations gives confidence that our sample is reliably capturing the underlying behaviour.

The right-hand panel of Fig. 2 shows the same data but now split by our morphology classification. Unfortunately, the number of 'blue sequence' galaxies drops off dramatically above 10^{11} M$_\odot$, which is where the significant increase in *ex situ* fraction with mass becomes apparent for the full sample. However, within the stellar mass range where both galaxy types have sufficient numbers for analysis ($M_* < 10^{11}$ M$_\odot$), there is a statistically significant difference in the two distributions (the Kolomogorov–Smirnov test gives a p-value of $p < 10^{-6}$, therefore the hypothesis that the samples come from the same distributions can be rejected). This difference is characterized in the sense that blue sequence galaxies have a lower *ex situ* fraction compared to red sequence galaxies of the same mass. This finding is consistent with that of Rodriguez-Gomez et al. (2016), who found a similar trend for Illustris galaxies.

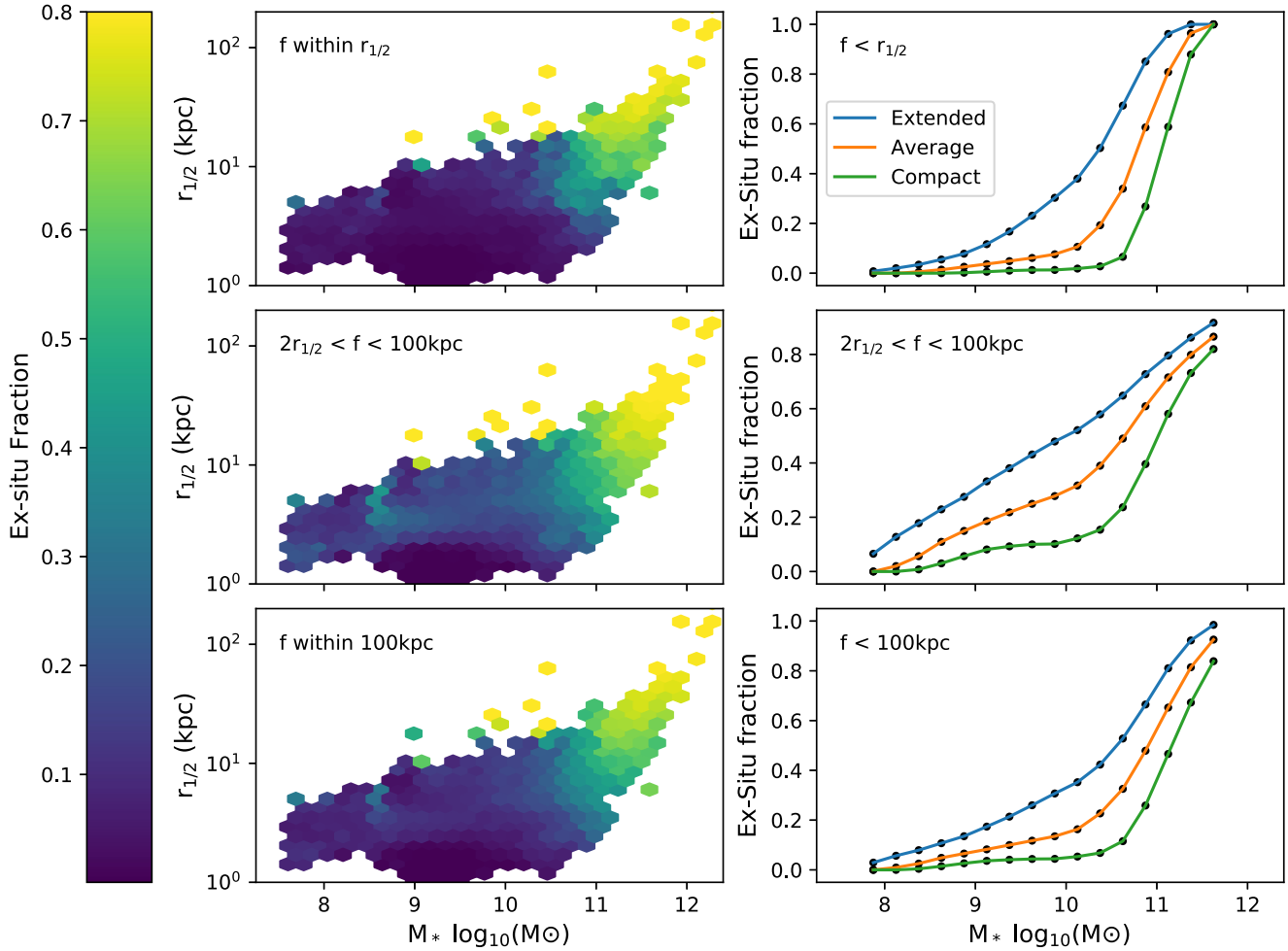

Figure 3. On the left-hand panels, binned $z = 0$ simulated galaxies are shown on the mass–size plane with colouration by *ex situ* fraction. The upper left panel limits to only star particles up to $r_{1/2}$, and the middle left panel limits to all particles outside of 2 $r_{1/2}$ ($r < 100$ pkpc). Finally, the lower left panel includes all particles within an aperture of 100 pkpc. The panels use a 2D LOESS smoothing function to remove small fluctuations, and to better display the general trend. Colour is given by the median of *ex situ* values within a hexagonal bin, with a minimum of three objects in a bin, a maximum of 1007 objects in a bin, and an average of 57 objects in a bin. The right-hand panels show mass against *ex situ* fraction, when separated into three bins of galaxy radius at fixed mass. The 'Extended' line collects the upper 33 per cent of particles spatially on the y-axis. The 'Average' line represents the central 33 per cent and the 'Compact' line collects the lowest 33 per cent of objects. The stellar mass axis is binned into 0.25 dex bins, with a minimum of 17 objects in a bin.

3.1.2 Ex situ fractions across the mass–size plane

We next examine the behaviour of the *ex situ* fraction across the galaxy mass–size plane. To display this information, data are projected on to mass–size axes with colour denoting the *ex situ* fraction. The great variety in the density of the galaxies across the mass–size plane is mitigated using a tessellated hexagonal binning approach. Bins are adjusted such that they remain of equal size on log–log axes. Galaxies falling within each bin are identified, and the median of the *ex situ* fraction for all galaxies within the bin is calculated. Bins have a minimum of three galaxies, and the most populated bin contains 1007 galaxies.

We separate particles by radial location within a galaxy, respective to the half-mass radius $r_{1/2}$. In the upper left panel of Fig. 3, we show the *ex situ* fraction of particles within $r_{1/2}$, and in the centre left panel only particles with a distance from the galaxy centre greater than 2 $r_{1/2}$ ($r < 100$ pkpc). Finally, in the lower left panel, we show all particles within an aperture of 100 pkpc. A LOESS smoothing function (Cappellari et al. 2013) is applied to the image, this implements 2D local adaptive smoothing across the plane (Cleveland & Devlin 1988) to reduce the influence of outlier points.

Examination of Fig. 3 reaffirms the finding from Fig. 2 that as stellar mass increases, so does *ex situ* fraction. This trend is clearly present for stars in both the inner and outer regions of galaxies, though clearly *ex situ* stars comprise a larger fraction of those found at larger radii. This finding is therefore consistent with those of previous studies that indicate that the majority of *ex situ* stars are deposited on the outer regions of galaxies (see e.g. Oser et al. 2010; Rodriguez-Gomez et al. 2016).

As a further extension to this analysis, we also examine potential relations between *ex situ* fraction and galaxy size. To do this at fixed mass, we split the galaxy population into three equal bins (by number of galaxies) of galaxy radius, and then calculate the median *ex situ* fraction for each bin. These median lines represent the 33 per cent most extended, 33 per cent most compact, and 33 per cent most intermediate radius galaxies, respectively. The radii separated by the bins vary with stellar mass, such that there are always a third of the galaxies at fixed mass within each bin. The right-hand panels of

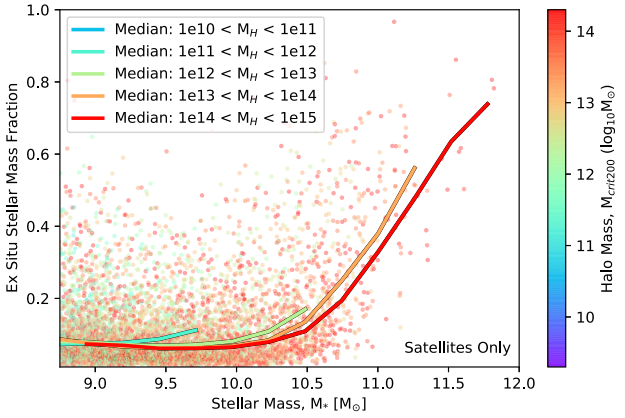

Figure 4. *Ex situ* fraction within 100 pkpc for all $z = 0$ satellite galaxies with >500 stellar particles against stellar mass, and split by total halo mass. Individual objects are coloured by the mass of the halo to which they belong. Solid lines show the median position of the *ex situ* fraction for objects within five bins of parent halo mass, across 0.25 dex wide bins of stellar mass. There are a minimum of five objects per bin, and an average of 220 objects per bin.

Fig. 3 show the result of this procedure. As can be clearly seen, there is a distinct separation of the median *ex situ* fractions of compact, mid-sized, and extended galaxies, for all galaxies at all masses. This separation is apparent both for the stars contained within $r_{1/2}$, and even more so for those beyond 2 $r_{1/2}$.

The fact that at fixed mass, more extended galaxies exhibit higher *ex situ* mass fraction supports the idea that they are larger because they accreted more stars during generally 'dry' mergers after the initial burst of *in situ* star formation that formed the inner regions of the galaxy. The stars accreted during galaxy–galaxy mergers or fly-by interactions will preferentially be deposited at larger radii leading to an increase in the half-mass radius of the galaxy (see e.g. Oser et al. 2010; Rodriguez-Gomez et al. 2016). In contrast, gas accreted during 'wet' galaxy interactions can find its way to the inner regions of the galaxy, as it is dissipative. There it can increase the number and density of *in situ* stars, potentially even decreasing the half-mass radius of the galaxy (see e.g. Du et al. 2019).

3.1.3 *Ex situ fraction as a function of parent halo mass*

To probe for differences in *ex situ* fraction with halo mass, we next limit the sample to include only satellite galaxies (with >500 stellar particles) and separate by the mass of the halo they reside in. Fig. 4 shows the result of this analysis for all satellites. Analysis was also performed for the centrals only. Though similar effects as discussed below were present, statistical resolution was strained and so the analysis was excluded from this study. We see in Fig. 4 that *ex situ* fraction appears to be highest in objects with a lower parent halo mass, becoming especially distinct at $\sim M_* > 10^{10.5}$ M$_\odot$. At first glance this may seem counterintuitive, considering that one might reasonably expect more merger activity within denser environments such as those of rich clusters. However, such trends have been hinted at in previous analyses, for example in Pillepich et al. (2018), where their fig. 12 shows a similar flattening of the *ex situ* fraction increase for the most massive haloes, and indeed a drop in *ex situ* fraction for stars in the inner regions of galaxies in the highest mass haloes.

Possible mechanisms for this effect are discussed in Section 4. Further clarifications of the robustness of this result with respect to known Subfind issues are found in Appendix.

The fact that we observe significant differences in *ex situ* fraction as a function of parent halo mass suggests a possible explanation for the observation that blue sequence galaxies display lower *ex situ* fraction than red sequence galaxies of the same stellar mass (see Fig. 2); that it is the result of the red sequence galaxies living preferentially in denser regions. To test this hypothesis we undertake the following test; we produce samples of red and blue sequence galaxies in fixed stellar mass bins that have the same halo stellar mass distribution. In practice this means that within each stellar mass bin, we randomly subselect red sequence galaxies (that are more common in the simulations), to match the observed halo mass distribution of the blue galaxies. In the rare cases where no red sequence galaxy of the appropriate stellar mass has the parent halo mass of a particular blue sequence galaxy, both galaxies are removed from their respective samples. Though this significantly reduces the number of objects available in the subset, the halo distributions match one-to-one.

With this subset, we repeat the same analysis as Section 3.1.1 as a function of stellar mass for both galaxy types. This allows us to examine whether samples of early- and late-type galaxies, matched in mass and halo mass, still display different *ex situ* fractions. In Fig. 5, we see that the new subselected sample shows no preference for higher or lower *ex situ* fraction compared to the original sample. Thus persists the systematic trend that early types have a larger *ex situ* fraction. We employ 50 Monte Carlo simulations to estimate error from our random selection, and all original positions are well within these errors. This is possibly a result of the large uncertainties in *ex situ* fraction, though the general trends are highly consistent. As a result, we can be reasonably sure that the differences in *ex situ* fraction between red and blue galaxies at fixed mass do not appear to be driven by systematic differences in halo mass distribution.

3.2 *Ex situ* fraction across galaxies' bodies

3.2.1 *Ex situ fraction as a function of radius*

We produce an analysis of all galaxies of >500 particles as a function of individual subhalo galactocentric distance. When binned by stellar mass, this allows us to see the increase of *ex situ* fraction with radius, for each stellar mass bin. This is shown in Fig. 6.

From Fig. 6, we see that for less massive galaxies (10^9–10^{10} M$_\odot$) not only does the mass fraction of *ex situ* stars increase with galactocentric radius, so does the rate of increase. For more massive galaxies (10^{11}–10^{12} M$_\odot$), the *ex situ* fraction increase is linear with galactocentric radius, with even the most central regions containing an average *ex situ* fraction of >65 per cent. This can also be seen in the Illustris simulations, as is shown by Rodriguez-Gomez et al. (2016) in their fig. 10.

3.2.2 *Ex situ fraction as a function of surface brightness*

By linking the *ex situ* fraction to the surface brightness (described in Section 2.5), we create an observationally comparable parameter. This allows us to create predictions of *ex situ* fraction that are verifiable observationally. The calculated surface brightness is paired with mass and size parameters of the simulated galaxies, adding a further dimension to the plots. Similarly to the analysis performed to investigate halo mass effects, the galaxies are split by stellar mass. Fig. 7 shows the separation of EAGLE galaxies by mass, along with their average position in the surface brightness/*ex situ* fraction plane.

The figure shows a mostly low *ex situ* fraction, while surface brightness increases up to a stellar mass of 10^{10}–10^{11} M$_\odot$. At this

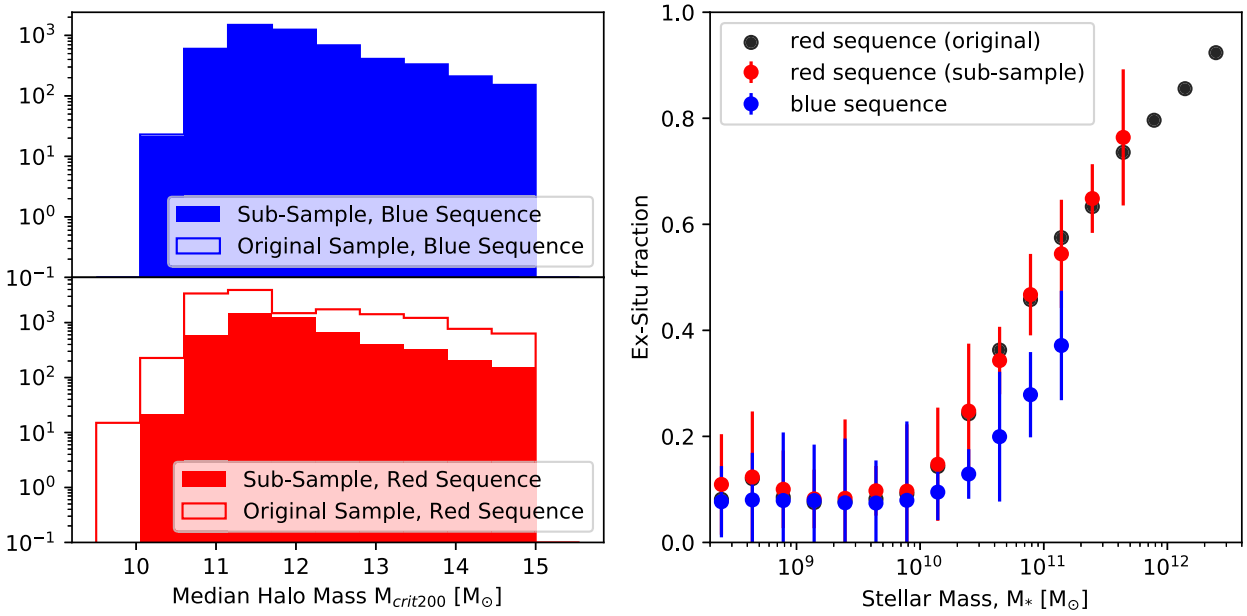

Figure 5. *Ex situ* fraction of subselected galaxies, such that the halo mass distributions of red and blue sequence samples match. Left-hand panels show original and new sample histograms. There are no residual differences between the two samples. The right-hand panel shows the results of the stellar mass *ex situ* distribution after the resampling with values binned in 0.25 dex bins of stellar mass. There is no significant difference between the original data set of red sequence galaxies, and the resampled data set of red sequence galaxies.

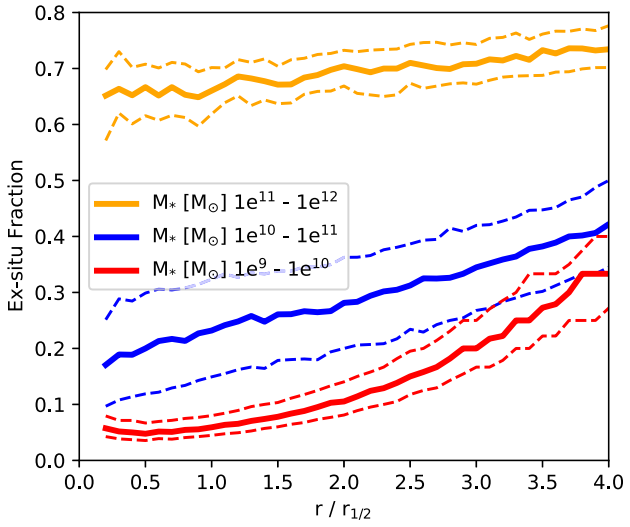

Figure 6. *Ex situ* fraction as a function of galactocentric radius, normalized to individual subhalo half-mass radius ($z = 0$). Galaxies are binned by total stellar mass. Solid lines show the average *ex situ* fraction for a galaxy within the stellar mass bin. Dashed lines show 1σ percentile lines of the *ex situ* scatter. Mean values are calculated from bins of size 0.1 $r_{1/2}$ with 6421 objects in the 10^9–10^{10} M$_\odot$ sample, 1418 objects in the 10^{10}–10^{11} M$_\odot$ sample, and 263 objects in the 10^{11}–10^{12} M$_\odot$ sample.

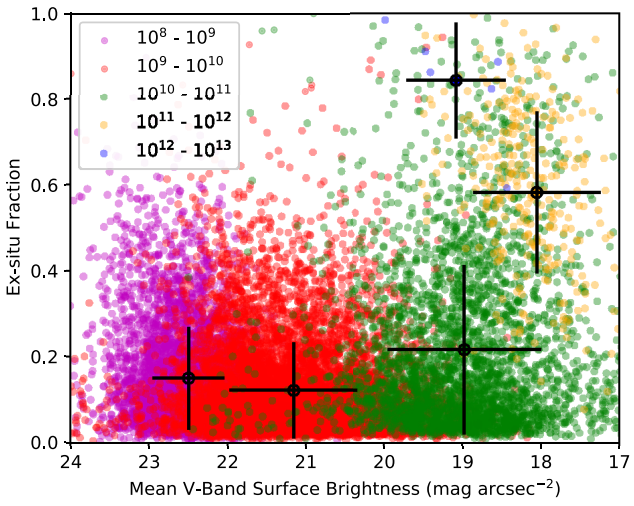

Figure 7. *Ex situ* fraction of the $z = 0$ EAGLE galaxies (centrals and satellites) as a function of mean *V*-band surface brightness within $r_{1/2}$, with separation by mass. The legend shows colour division of stellar mass ranges (M$_\odot$). Mean values are overplotted in a larger sized point with 1σ standard deviation bars attached. Note that points are plot in order of mass, thus overlapping regions are obscured by higher mass points.

turning point, as mass increases, surface brightness decreases, while *ex situ* fraction rises. This is consistent with our picture of galaxy evolution, in which average surface brightness within $r_{1/2}$ increases with stellar mass initially. Then beyond a stellar mass of $\sim 10^{10}$–10^{11} M$_\odot$ *ex situ* fraction begins to rapidly increase. As this occurs, the average surface brightness density decreases. This lends weight to the idea that *ex situ* stars are preferentially accreted to the outskirts, where they increase the half-light radius, extending the galaxy and thereby reducing the average surface brightness within the effective radius. This can be seen in Fig. 6 where high fractions of *ex situ* stars are present at large galactocentric radii compared with the galaxy centres.

We then move to generating predictions for the *ex situ* mass fraction as a function of galaxy mass and surface brightness. To ensure the generation of data easily comparable to observable galaxies, our analysis is performed by examining the *ex situ* fractions within radial bins containing like surface brightnesses.

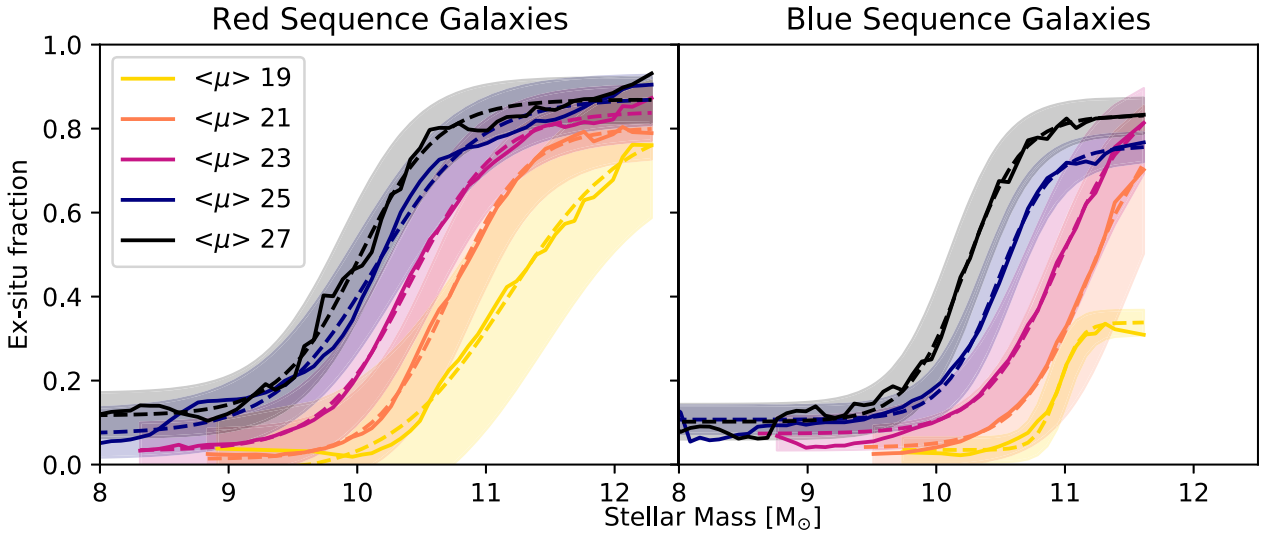

Figure 8. Mass and *ex situ* fraction for all $z = 0$ objects, considering only particles within integer magnitudes per square arcsecond projected ellipses in *V* band. Solid lines show the true data, dashed lines show a fitting function. Sigmoid functions are fit to the data as described in Section 3. Five different magnitudes per square arcsecond ($<\mu>$) bins are shown here, with additional values tabulated in Table 1. Shaded regions show the 1σ distribution of *ex situ* scatter.

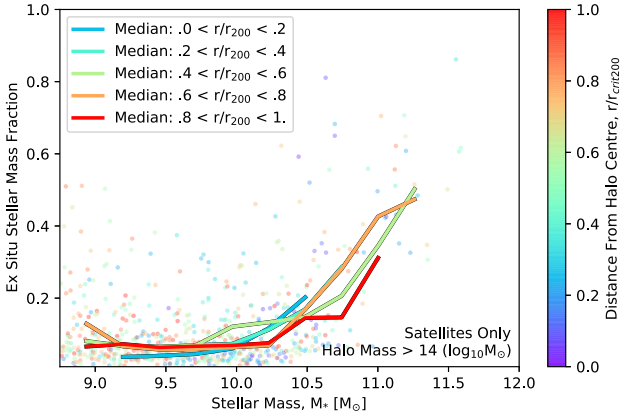

Figure 9. *Ex situ* fraction within 100 pkpc for $z = 0$ satellite galaxies with >500 stellar particles and where $M_* > 10^{14}$ M$_\odot$. *Ex situ* fraction is shown against stellar mass, and split by distance from the halo centre. Individual objects are coloured by the fraction of the distance from the centre of the halo to which they belong, between 0 and 1 $r/r_{\rm crit200}$. Solid lines show the median position of the *ex situ* fraction for objects within five bins of fractional radial location in the halo, across 0.25 dex wide bins of stellar mass. There are a minimum of three objects per bin, and an average of 14 objects per bin.

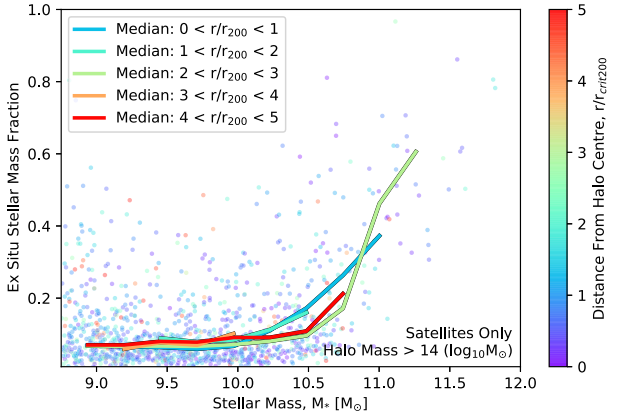

Figure 10. Ex situ fraction within 100 pkpc for $z = 0$ satellite galaxies with >500 stellar particles and where $M_* > 10^{14}$ M$_\odot$. Ex situ fraction is shown against stellar mass, and split by distance from the halo centre. Individual objects are coloured by the fraction of the distance from the centre of the halo to which they belong between 0 and 5 $r/r_{\rm crit200}$. Solid lines show the median position of the *ex situ* fraction for objects within five bins of fractional radial location in the halo, across 0.25 dex wide bins of stellar mass. There are a minimum of three objects per bin, and an average of 86 objects per bin.

Using the method described in Section 2.5, magnitudes per square arcsecond (calculated for an assumed distance of 16.5 Mpc, the approximate distance to the Virgo cluster) are linked to the *ex situ* fractions within the magnitude bins. These values are used to examine the median *ex situ* fraction with mass, for constant surface brightnesses.

This is shown in Fig. 8, where surface brightnesses of magnitudes 19–27 per square arcsec are considered for *V* band. Sigmoid functions are fit to the data of the form:

$$\frac{c}{1 + e^{-a(x-b)}} + d, \tag{10}$$

where *a, b, c*, and *d* are constants tabulated in Table 1. This allows the expected *ex situ* fraction at any stellar mass ($8 < \log_{10}(M_\odot) < 12.5$) to be calculated according to the function at a particular surface brightness. Shaded error bars show the 1σ scatter in the *ex situ* values within each bin, which are provided as a covariance matrix of the form shown below, where all elements are tabulated in Table 2.

$$\begin{bmatrix} \alpha & \beta & \gamma & \delta \\ \beta & \epsilon & \zeta & \eta \\ \gamma & \zeta & \theta & \iota \\ \delta & \eta & \iota & \kappa \end{bmatrix} \tag{11}$$

The purpose of this plot, and the tabulated constants is to provide predictions that may be compared directly to forthcoming observational studies. Tabulated constant values are shown in Table 1 for surface brightnesses of 19–27 mag per square arcsec for *V* band. Values for filters Johnson–Cousins *V*, *B*, and *R*; and Sloan *g*, *r*, and *i*, are also available as supplementary material online.

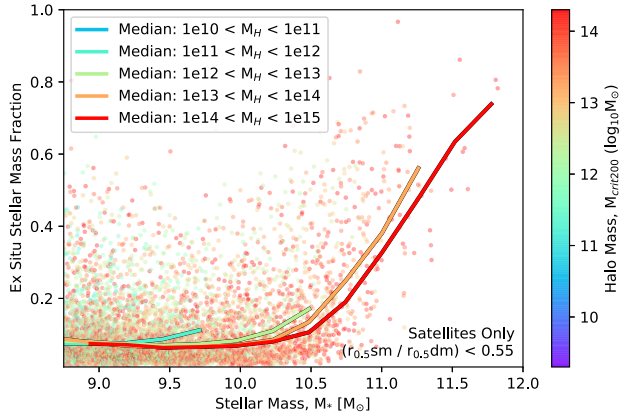

Figure 11. *Ex situ* fraction within 100 pkpc for all $z = 0$ satellite galaxies with >500 stellar particles where $r_{sm0.5}/r_{dm0.5}) < 0.55$. *Ex situ* fraction is shown against stellar mass, and split by total halo mass. Individual objects are coloured by the mass of the halo to which they belong. Solid lines show the median position of the ex situ fraction for objects within five bins of parent halo mass, across 0.25 dex wide bins of stellar mass. There are a minimum of five objects per bin, and an average of 220 objects per bin.

Table 1. Constants for *V*-band surface brightness to *ex situ* fraction functions for the stellar mass range $8 < \log_{10}M_\odot < 12.5$ in equation (10). Surface brightnesses (μ_V) of 19–27 mag per square arcsec are shown.

μ_V	*a*	*b*	*c*	*d*
Red sequence galaxies				
19	2.252	11.135	0.842	−0.030
20	3.050	10.892	0.788	−0.006
21	3.534	10.732	0.790	0.010
22	3.461	10.645	0.795	0.031
23	3.458	10.509	0.801	0.034
24	3.535	10.419	0.787	0.054
25	3.507	10.309	0.783	0.073
26	3.219	10.151	0.780	0.085
27	2.886	10.009	0.756	0.110
Blue sequence galaxies				
19	12.756	10.960	0.302	0.037
20	14.823	10.946	0.305	0.082
21	3.490	11.185	0.852	0.025
22	2.838	11.258	1.142	0.027
23	2.663	11.040	0.975	0.034
24	3.574	10.653	0.740	0.054
25	4.713	10.502	0.655	0.098
26	4.242	10.375	0.709	0.086
27	5.161	10.157	0.671	0.102

4 DISCUSSION

In this study, we explore the relation of *ex situ* material to galaxy properties, both global and local. In Fig. 2, we plot stellar mass against *ex situ* fraction. An increase in *ex situ* fraction with stellar mass matches existing expectations (drawn from complementary simulations) about galaxies of larger mass possessing greater fractions of stars accreted from other galaxies. Likewise, less massive galaxies have been shown to have few or even no *ex situ* stars (Fitts et al. 2018). When all galaxies are considered, at the highest mass bin limits, the average *ex situ* fraction reaches as high as ≈84.2 per cent. This almost identical to the fraction recovered at the highest mass bin by Rodriguez-Gomez et al. (2016) for the Illustris simulations as discussed in Section 3.1.1.

When comparing to other analyses of the EAGLE simulations, we see small differences between those results and our own. A likely reason for the small differences between analyses of the same simulation is due to differences in *ex situ* and *in situ* classification. In our method we trace all particles through their entire merger history from formation to $z = 0$, resulting in identification of origin. It is possible for a few particles to be mistakenly labelled as *ex situ* when swapping between subhaloes during mergers, however, this possible overestimation of *ex situ* fraction is negligible and does not impact on the statistics of our sample.

A second parameter with trends in *ex situ* fraction was found to be the total mass of the halo that hosts a satellite galaxy. By forming a subsample of satellite galaxies split by the mass of their parent halo, we were able to compare the effects of halo mass on *ex situ* fraction. As seen in Fig. 4 there is a variation with halo mass such that satellite galaxies within the most massive haloes possess consistently lower *ex situ* fractions on average compared to those of the same stellar mass in the next lowest halo mass bin. Objects within intermediate mass haloes ($M*_{halo} > 1 \times 10^{13}$ M$_\odot$) seem to experience especially efficient accretion of stars on to galaxies.

As a general rule, at fixed stellar mass, satellite galaxies residing in higher mass haloes have lower *ex situ* fraction within 100 kpc. This is unexpected when we consider the vastly larger potential wells of larger and likely older haloes. The effect is also visible in similar environmental analyses of other simulations, such as in fig. 12 of Pillepich et al. (2018), in which the IllustrisTNG simulation shows the same effect. Though present in the plot, this is not commented upon, possibly due to the subtle nature of the effect.

Initially the proposed explanation for this effect was as the result of overcooling Crain et al. (2015), in which the most massive haloes cease to display efficient AGN feedback, leading to artificially high *in situ* fractions. This was eliminated as a potential mechanism by running the same analyses, though ignoring stars born after $z = 1$. The result shows the same effect as in Fig. 4 in which satellite galaxies within the more massive haloes contain an *ex situ* fraction that is lower than galaxies of the same mass in less massive haloes. As such, we can expect there to be more mechanisms responsible than purely overcooling.

A number of mechanisms could be responsible for the effect that satellite galaxies within higher mass haloes have lower *ex situ* fraction. One is that because passing velocities in clusters are so high, true mergers are rare, and it becomes more likely that material gets pulled out and added to the intracluster light (ICL) than actually incorporated into another galaxy (Moore et al. 1996; Makino & Hut 1997). In contrast, within groups the passing velocities are lower and mergers are more likely (Bahcall, Gramann & Cen 1994). Although, we might expect clusters to be built from groups and thus have a similar fraction, it is possible we are instead seeing an influence of survivor bias. This could occur where groups that fell into clusters did so, on average, long ago and ceased merging, whereas surviving groups today have had much longer to continue to merge.

Evidence for this mechanism can be found in literature (e.g. Gu et al. 2018) where stellar population models are fit to spectra of ICL. The velocity dispersion of the stars indicate that many ICL stars are dissociated from individual galaxies and are instead influenced by the gravitational potential of the cluster as a whole. The authors of the study suggest tidal stripping as a potential formation mechanism for the ICL, where fly-bys of massive galaxies can expel significant amounts of matter into the Intra-Cluster Medium (ICM).

Table 2. Constants for *V*-band covariance matrix (equation 11) to surface brightness functions for the stellar mass range $8 < \log_{10}M_{\odot} < 12.5$. Surface brightnesses ($\mu_V$) of 19–27 mag per square arcsec are shown.

μ_V	α	β	γ	δ	ϵ	ζ	η	θ	ι	κ
Red sequence galaxies										
19	3.919	−0.281	−0.776	0.287	0.141	7.11E-02	6.86E-03	0.177	0.177	3.33E-02
20	4.972	−0.041	−0.448	0.207	0.060	5.81E-03	1.33E-02	0.057	0.057	1.85E-02
21	5.670	−0.041	−0.315	0.138	0.043	4.60E-03	8.11E-03	0.032	0.032	1.07E-02
22	5.076	−0.048	−0.270	0.112	0.043	5.40E-03	6.98E-03	0.028	0.028	8.89E-03
23	4.735	−0.046	−0.226	0.091	0.041	5.04E-03	6.06E-03	0.023	0.023	7.41E-03
24	4.607	−0.057	−0.180	0.063	0.038	5.77E-03	4.22E-03	0.018	0.018	5.00E-03
25	4.534	−0.046	−0.171	0.065	0.039	4.61E-03	4.56E-03	0.017	0.017	5.20E-03
26	3.665	−0.029	−0.163	0.069	0.043	3.18E-03	5.78E-03	0.017	0.017	6.06E-03
27	2.945	−0.012	−0.161	0.076	0.052	1.49E-03	7.71E-03	0.018	0.018	7.16E-03
Blue sequence galaxies										
19	220.933	−0.256	−0.769	0.219	0.011	2.72E-03	1.19E-03	0.008	−0.002	1.88E-03
20	439.691	−0.331	−1.018	0.259	0.012	2.97E-03	1.15E-03	0.009	−0.002	2.01E-03
21	9.661	−1.224	−1.852	0.169	0.225	3.03E-01	−1.35E-02	0.449	−0.030	6.45E-03
22	5.746	−1.500	−2.413	0.129	0.497	7.72E-01	−2.43E-02	1.245	−0.048	6.31E-03
23	4.264	−0.985	−1.273	0.100	0.321	3.75E-01	−1.46E-02	0.475	−0.028	5.56E-03
24	5.745	−0.343	−0.457	0.065	0.061	4.38E-02	3.19E-04	0.055	−0.007	3.32E-03
25	10.459	−0.202	−0.326	0.057	0.030	1.37E-02	1.45E-03	0.021	−0.003	2.48E-03
26	7.935	−0.172	−0.303	0.063	0.034	1.39E-02	2.02E-03	0.024	−0.005	3.34E-03
27	13.924	−0.125	−0.306	0.080	0.026	7.37E-03	2.39E-03	0.018	−0.004	3.63E-03

Another mechanism for this effect could be partly due to differences in galaxy formation efficiency driven by assembly bias. At fixed halo mass, galaxies that form earlier do so more efficiently, because the central density is higher and outflows find it harder to escape (Gunn & Gott 1972). As such, earlier forming galaxies end up with a higher M_*/Msub ratio, where Msub is the stellar mass contained in solely subhaloes. The satellites of the most massive clusters will have formed the earliest on average, since they are part of higher sigma peaks, and so these could be systematically more efficient at star formation. At fixed M_*, we are then looking at systematically lower subhalo mass fractions (as a fraction of the halo mass) as we transition from groups to clusters, and as such you could expect a lower *ex situ* fraction.

By separating galaxies based on their half-mass radius, we investigate and compare spatial differences regardless of galaxy size. The increase in *ex situ* fraction (as seen in Fig. 3) is present both in the central ($<r_{1/2}$) region and outer regions ($>2\ r_{1/2}$). For both central and outer regions this is the case at all masses, though *ex situ* fraction increases negligibly with extent for central regions below a mass of $M_* < 5 \times 10^8$ M$_{\odot}$. This situation is perhaps to be expected, as higher mass haloes are thought to be assembled through a higher fraction of mergers (Maller et al. 2006).

When looking solely at the central region of galaxies, more diffuse galaxies have accreted a higher fraction of stars than their denser counterparts. This difference is as equally pronounced for the outer regions of the same galaxies, with fractions between 5 and 30 per cent greater at all masses where $M_* > 5 \times 10^8$ M$_{\odot}$. The increase in *ex situ* fraction at all masses for the outer regions is indicative of stripped *ex situ* stars preferentially remaining in the disc and halo and infrequently migrating to the core. This is supportive of the 'two phase' scenario wherein an initial core of *in situ* stars accretes stars via mergers and tidal stripping.

Once above $M_* > 2 \times 10^9$ M$_{\odot}$, the *ex situ* fraction of the outer regions quickly surpasses 50 per cent for the most diffuse galaxies, and all galaxies of mass $M_* > 2 \times 10^{11}$ M$_{\odot}$ contain more than 50 per cent constituent *ex situ* stars, regardless of radius.

Future observational techniques will likely independently estimate *ex situ* fractions, with the novel techniques as described in Section 1. Fig. 8 converts the simulated data into predictions that may be more readily compared with these future observational estimates.

5 CONCLUSIONS

We have analysed two EAGLE simulations of volumes 25 and 100 cMpc^3 within the sample stellar mass range of (2×10^7–1.9×10^{12} M$_{\odot}$) for both central and satellite galaxies. From these, we have extracted *ex situ* fraction information at $z = 0$ with respect to spatially resolved galaxy parameters. We have investigated how *ex situ* fraction changes with stellar mass, and at fixed mass with changes in half-mass radius. Furthermore, we have examined *ex situ* changes with group/cluster halo mass by separating satellite galaxies by the mass of the group/cluster halo they reside in. Lastly, we have used mass-to-light ratios to determine the expected *ex situ* fractions for galaxies at a specific mass and surface brightness value.

Our main findings are summarized as follows:

(i) We find that more massive galaxies gain proportionally more stellar mass from *ex situ* sources. This is in common with previous findings in literature (e.g. Oser et al. 2010; Rodriguez-Gomez et al. 2016; Qu et al. 2017; Pillepich et al. 2018). For the most massive galaxies included in the sample ($>1 \times 10^{12}$ M$_{\odot}$), *ex situ* fraction was found to be, on average, >80 per cent; and for individual cases at these masses the *ex situ* fraction could be as high as >90 per cent.

(ii) At fixed galaxy mass, when separated by its parent group/cluster halo mass, there is a consistently lower *ex situ* fraction for satellite galaxies within the highest mass group/cluster haloes. One interpretation of this is that the high passing velocities present in massive clusters disfavours true mergers and stellar accretion. Instead of material being added to a galaxy during a close pass/merger, the material is instead removed from the original galaxy and spread amongst the ICM. Another interpretation is that the effect is the result of differences in feedback efficiency with time, where tightly bound group/cluster haloes possess denser circumgalactic medium as a result of less efficient feedback. This in turn causes a higher rate of *in situ* formation. Similar effects were seen in analysis of a purely central sample, however, statistics were too poor to explore

this result with any certainty. This remains a point of investigation for larger samples in the future.

(iii) At all galaxy stellar masses, there is an increase in *ex situ* fraction with increasing galaxy stellar size, thus showing how at fixed mass, more diffuse galaxies are more likely to contain a greater *ex situ* fraction. This supports the idea that physically more extended galaxies are more extended because they have accreted more material preferentially on to their outskirts. This is especially clear in the right-hand panels of Fig. 3 where bins of the most diffuse, most compact and average galaxies remain separated from the lowest until the very highest mass extent of the simulation.

(iv) We have also produced predictions for the accreted fraction as a function of galaxy mass and surface brightness. These predictions show estimated *ex situ* fractions for the same sample of galaxies, but limited to elliptical isophotes of specific surface brightness values. Combined with stellar mass, these can be used to estimate the *ex situ* fraction for observed galaxies of similar surface brightness and mass. This can also be readily compared to observational data processed by new analytic techniques such as recently advanced full spectral fitting methods, for both spatially resolved, and non-spatially resolved galaxies. See Table 1 for the tabulated data for *V* band. Other bands are also available.

ACKNOWLEDGEMENTS

The authors gratefully acknowledge insightful and constructive comments from the anonymous referee. This work was completed with support from the ESO Studentship Programme, the Isaac Newton Group of Telescopes Studentship as well as the Moses Holden Studentship, with particular thanks to Patrick Holden. JJD and RAC acknowledge financial support from the Royal Society. JP gratefully acknowledges financial support from the European Research Council (ERC-CoG-646928, Multi-Pop).

DATA AVAILABILITY

The data underlying this article are available in the EAGLE public data release at http://icc.dur.ac.uk/Eagle/database.php

REFERENCES

Bacon R. et al., 2001, MNRAS, 326, 23
Bacon R. et al., 2010, in McLean I. S., Ramsay S. K., Takami H., eds, Proc. SPIE Conf. Ser. Vol. 7735, Ground-Based and Airborne Instrumentation for Astronomy III. SPIE, Bellingham, p. 773508
Bahcall N. A., Gramann M., Cen R., 1994, ApJ, 436, 23
Beasley M. A., Trujillo I., Leaman R., Montes M., 2018, Nature, 555, 483
Belokurov V. et al., 2006, ApJ, 642, L137
Boecker A., Leaman R., van de Ven G., Norris M. A., Mackereth J. T., Crain R. A., 2019, MNRAS, 491, 823
Cappellari M., 2017, MNRAS, 466, 798
Cappellari M., Emsellem E., 2004, PASP, 116, 138
Cappellari M. et al., 2013, MNRAS, 432, 1862
Chabrier G., 2003, PASP, 115, 763
Cid Fernandes R., Mateus A., Sodré L., Stasińska G., Gomes J. M., 2005, MNRAS, 358, 363
Clauwens B., Schaye J., Franx M., Bower R. G., 2018, MNRAS, 478, 3994
Cleveland W. S., Devlin S. J., 1988, J. Am. Stat. Assoc., 83, 596
Correa C. A., Schaye J., Clauwens B., Bower R. G., Crain R. A., Schaller M., Theuns T., Thob A. C. R., 2017, MNRAS, 472, L45
Crain R. A. et al., 2015, MNRAS, 450, 1937
Du M. et al., 2019, ApJ, 875, 58
Dubois Y. et al., 2014, MNRAS, 444, 1453
Fahrion K. et al., 2020, A&A, 637, A27
Ferré-Mateu A., Trujillo I., Martín-Navarro I., Vazdekis A., Mezcua M., Balcells M., Domínguez L., 2017, MNRAS, 467, 1929
Fitts A. et al., 2018, MNRAS, 479, 319
Forbes D. A., Spitler L. R., Strader J., Romanowsky A. J., Brodie J. P., Foster C., 2011, MNRAS, 413, 2943
Furlong M. et al., 2015, MNRAS, 450, 4486
Furlong M. et al., 2016, MNRAS, 465, 722
Genel S. et al., 2014, MNRAS, 445, 175
Greene J. E., Murphy J. D., Comerford J. M., Gebhardt K., Adams J. J., 2012, ApJ, 750, 32
Gu M. et al., 2020, ApJ, 894, 32
Guérou A., Emsellem E., Krajnović D., McDermid R. M., Contini T., Weilbacher P. M., 2016, A&A, 591, A143
Gunn J. E., Gott J. R. III, 1972, ApJ, 176, 1
Hill G. J. et al., 2008, in McLean I. S., Casali M. M., eds, Proc. SPIE Conf. Ser. Vol. 7014, Ground-Based and Airborne Instrumentation for Astronomy II. SPIE, Bellingham, p. 701470
Hood C. E., Kannappan S. J., Stark D. V., Dell'Antonio I. P., Moffett A. J., Eckert K. D., Norris M. A., Hendel D., 2018, ApJ, 857, 144
Hopkins P. F., Kereš D., Oñorbe J., Faucher-Giguère C.-A., Quataert E., Murray N., Bullock J. S., 2014, MNRAS, 445, 581
Jennings Z. G. et al., 2015, ApJ, 812, L10
Jiang L., Helly J. C., Cole S., Frenk C. S., 2014, MNRAS, 440, 2115
Kacharov N., Neumayer N., Seth A. C., Cappellari M., McDermid R., Walcher C. J., Böker T., 2018, MNRAS, 480, 1973
Knebe A. et al., 2011, MNRAS, 415, 2293
Krajnović D., Cappellari M., McDermid R. M., 2018, MNRAS, 473, 5237
Kruijssen J. M. D., Pfeffer J. L., Reina-Campos M., Crain R. A., Bastian N., 2018, MNRAS, 486, 3180
Kruijssen J. M. D., Pfeffer J. L., Crain R. A., Bastian N., 2019, MNRAS, 486, 3134
La Barbera F., Ferreras I., de Carvalho R. R., Bruzual G., Charlot S., Pasquali A., Merlin E., 2012, MNRAS, 426, 2300
Lackner C. N., Cen R., Ostriker J. P., Joung M. R., 2012, MNRAS, 425, 641
Lagos C. d. P. et al., 2015, MNRAS, 452, 3815
Lagos C. d. P., Schaye J., Bahé Y., Van de Sande J., Kay S. T., Barnes D., Davis T. A., Dalla Vecchia C., 2018, MNRAS, 476, 4327
Lange R. et al., 2015, MNRAS, 447, 2603
Ludlow A. D., Schaye J., Schaller M., Richings J., 2019, MNRAS, 488, L123
Makino J., Hut P., 1997, ApJ, 481, 83
Maller A. H., Katz N., Kereš D., Davé R., Weinberg D. H., 2006, ApJ, 647, 763
Maraston C., 2005, MNRAS, 362, 799
Martin G., Kaviraj S., Devriendt J. E. G., Dubois Y., Pichon C., 2018, MNRAS, 480, 2266
Martínez-Delgado D., Peñarrubia J., Gabany R. J., Trujillo I., Majewski S. R., Pohlen M., 2008, ApJ, 689, 184
McAlpine S. et al., 2016, Astron. Comput., 15, 72
McGaugh S. S., Schombert J. M., 2014, AJ, 148, 77
Mentz J. J. et al., 2016, MNRAS, 463, 2819
Monachesi A. et al., 2019, MNRAS, 485, 2589
Moore B., Katz N., Lake G., Dressler A., Oemler A., 1996, Nature, 379, 613
Nelson D. et al., 2015, Astron. Comput., 13, 12
Norris M. A., Escudero C. G., Faifer F. R., Kannappan S. J., Forte J. C., van den Bosch R. C. E., 2015, MNRAS, 451, 3615
Norris M. A. et al., 2016, ApJ, 832, 198
Onodera M. et al., 2012, ApJ, 755, 26
Oser L., Ostriker J. P., Naab T., Johansson P. H., Burkert A., 2010, ApJ, 725, 2312
Pillepich A., Madau P., Mayer L., 2015, ApJ, 799, 184
Pillepich A. et al., 2018, MNRAS, 475, 648
Poci A., McDermid R. M., Zhu L., van de Ven G., 2019, MNRAS, 487, 3776
Pota V. et al., 2015, MNRAS, 450, 1962
Qu Y. et al., 2017, MNRAS, 464, 1659
Querejeta M. et al., 2015, A&A, 579, L2
Rodriguez-Gomez V. et al., 2016, MNRAS, 458, 2371

Romanowsky A. J., Strader J., Brodie J. P., Mihos J. C., Spitler L. R., Forbes D. A., Foster C., Arnold J. A., 2012, ApJ, 748, 29
Ruiz-Lara T. et al., 2018, MNRAS, 478, 2034
Sales L. V., Navarro J. F., Schaye J., Dalla Vecchia C., Springel V., Booth C. M., 2010, MNRAS, 409, 1541
Schaye J. et al., 2015, MNRAS, 446, 521
Shen S., Mo H. J., White S. D. M., Blanton M. R., Kauffmann G., Voges W., Brinkmann J., Csabai I., 2003, MNRAS, 343, 978
Tacchella S. et al., 2019, MNRAS, 487, 5416
Thob A. C. R. et al., 2019, MNRAS, 485, 972
Tojeiro R., Heavens A. F., Jimenez R., Panter B., 2007, MNRAS, 381, 1252
Trayford J. W. et al., 2015, MNRAS, 452, 2879
van der Wel A. et al., 2014, ApJ, 788, 28
van Dokkum P. G. et al., 2014, ApJ, 791, 45
Vogelsberger M. et al., 2014a, MNRAS, 444, 1518
Vogelsberger M. et al., 2014b, Nature, 509, 177

SUPPORTING INFORMATION

Supplementary data are available at *MNRAS* online.

Table S1. Constants for *V*-band surface brightness to *ex situ* fraction functions for the stellar mass range $8 < \log_{10} M_{\odot} < 12.5$ in equation (10).
Table S2. Constants for *V*-band covariance matrix (equation 11) to surface brightness functions for the stellar mass range $8 < \log_{10} M_{\odot} < 12.5$.
Table S3. Constants for *B*-band surface brightness to *ex situ* fraction functions for the stellar mass range $8 < \log_{10} M_{\odot} < 12.5$ in equation (10).
Table S4. Constants for *B*-band covariance matrix (equation 11) to surface brightness functions for the stellar mass range $8 < \log_{10} M_{\odot} < 12.5$.
Table S5. Constants for *R*-band surface brightness to *ex situ* fraction functions for the stellar mass range $8 < \log_{10} M_{\odot} < 12.5$ in equation (10).
Table S6. Constants for R band co-variance matrix (equation 11) to surface brightness functions for the stellar mass range $8 < \log_{10} M_{\odot} < 12.5$.
Table S7. Constants for *g*-band surface brightness to *ex situ* fraction functions for the stellar mass range $8 < \log_{10} M_{\odot} < 12.5$ in equation (10).
Table S8. Constants for *g*-band covariance matrix (equation 11) to surface brightness functions for the stellar mass range $8 < \log_{10} M_{\odot} < 12.5$.
Table S9. Constants for *r*-band surface brightness to *ex situ* fraction functions for the stellar mass range $8 < \log_{10} M_{\odot} < 12.5$ in equation (10).
Table S10. Constants for *r*-band covariance matrix (equation 11) to surface brightness functions for the stellar mass range $8 < \log_{10} M_{\odot} < 12.5$.
Table S11. Constants for *i*-band surface brightness to *ex situ* fraction functions for the stellar mass range $8 < \log_{10} M_{\odot} < 12.5$ in equation (10).
Table S12. Constants for *i*-band covariance matrix (equation 11) to surface brightness functions for the stellar mass range $8 < \log_{10} M_{\odot} < 12.5$.

Please note: Oxford University Press is not responsible for the content or functionality of any supporting materials supplied by the authors. Any queries (other than missing material) should be directed to the corresponding author for the article.

APPENDIX

Many substructure identification algorithms, including the Subfind algorithm used here, struggle to identify self-bound substructures against high-density backgrounds. As shown by Knebe et al. (2011), this can result in the spurious 'loss' of mass from the outskirts of substructures as their orbit takes them close to the centre of their host halo. Since *ex situ* stellar mass is preferentially located in the outskirts of galaxies, this effect has the potential to induce a host halo mass dependence on the *apparent ex situ* fraction of satellites at fixed stellar mass.

To confirm that this was not a driving effect of the result in Fig. 4, we restricted a sample to all satellites embedded within haloes of mass $M_* > 10^{14}$ $M_{\odot}$ (solid red line of Fig. 4) that would include the most severely impacted galaxies by a potential misidentification issue. By binning galaxies by radial location, as a fraction of the halo radius ($r_{\rm crit200}$) we could investigate if there were discernible differences in *ex situ* fraction for satellites closer to the halo centre.

As shown in Figs 9 and 10 there is no impact on the results from any such misidentification effect in the samples used in this study.

This was further confirmed by excluding satellite galaxies in which the extent of the subhalo dark matter component was comparable to that of the stellar component. As a result of the greater extent of the dark matter compared to the stellar component, this Subfind issue would affect the dark matter earlier than for the stars. By excluding the satellites in which $(r_{\rm sm0.5}/r_{\rm dm0.5}) > 0.55$ (where $r_{\rm sm0.5}$ and $r_{\rm dm0.5}$ are the stellar and dark matter half mass radii, respectively), we confirmed that we continued to see the effect as seen in Fig. 4.

This is shown in Fig. 11 where the sample was restricted to satellites in which $(r_{\rm sm0.5}/r_{\rm dm0.5}) < 0.55$ (exclusion of 7.5 per cent of the original sample). The effect shown in Fig. 4 persists, where at a fixed mass, more massive haloes contain satellites of a lower *ex situ* fraction. Thus we can confirm that this is most likely a physical result of the simulation, rather than from numerical error.

This paper has been typeset from a TEX/LATEX file prepared by the author.